

Collective band structures in the ^{99}Tc nucleus

H. J. Li,^{1,2} Z. G. Xiao,^{1,3,*} S. J. Zhu,¹ M. Patial,² C. Qi,² B. Cederwall,² Z. Zhang,¹ R. S. Wang,¹ H. Yi,¹ W. H. Yan,¹ W. J. Cheng,¹ Y. Huang,¹ L. M. Lyu,¹ Y. Zhang,¹ X. G. Wu,⁴ C. Y. He,⁴ Y. Zheng,⁴ G. S. Li,⁴ C. B. Li,⁴ H. W. Li,⁴ J. J. Liu,⁴ P. W. Luo,⁴ S. P. Hu,⁴ J. L. Wang,⁴ and Y. H. Wu⁴

¹Department of Physics, Tsinghua University, Beijing 100084, People's Republic of China

²Department of Physics, Royal Institute of Technology, SE-10691 Stockholm, Sweden

³Collaborative Innovation Center of Quantum Matter, Beijing 100084, China

⁴China Institute of Atomic Energy, Beijing 102413, People's Republic of China

(Received 21 November 2014; revised manuscript received 20 March 2015; published 14 May 2015)

Excited states in ^{99}Tc with energies up to 6 MeV have been populated using the $^{96}\text{Zr}(^7\text{Li}, 4n)^{99}\text{Tc}$ reaction with a laboratory beam energy of 35 MeV. Coincident γ rays from excited nuclei produced in the reactions were detected using an array of coaxial, planar, and clover-type high-purity germanium detectors. A total of 60 new γ -ray transitions and 21 new levels are identified and placed into a new level scheme. Two collective bands assigned to be built on the $\pi g_{9/2}[422]5/2^+$ and $\pi p_{1/2}[301]1/2^-$ Nilsson configurations have been extended with spins up to $35/2$ and $33/2 \hbar$, respectively. Backbending and signature inversion have been observed in the yrast band. The large signature splitting of the positive-parity band in ^{99}Tc may be caused by a triaxial deformation, which agrees well with the electromagnetic properties, theoretical calculations based on total Routhian surface, and triaxial particle-rotor model calculations.

DOI: [10.1103/PhysRevC.91.054314](https://doi.org/10.1103/PhysRevC.91.054314)

PACS number(s): 21.10.Re, 23.20.Lv, 27.60.+j, 25.70.Gh

I. INTRODUCTION

Nuclear shapes are determined by a complicated interplay of quantum many-body correlations. Most deformed nuclei have been interpreted to possess rotational properties consistent with axially symmetric shapes in their ground state and at low angular momentum. Axial asymmetry or triaxiality is a somewhat elusive phenomenon which was proposed to appear in nuclear regions like $A \sim 110$ [1–4], $A \sim 70$ [5–7], and $A \sim 160$ [8,9]. Triaxiality may manifest itself in transitional nuclei with the appearance of γ bands [10,11], wobbling motion at high angular momentum [10], enhanced signature splitting or even signature inversion [11]. Of particular interest is the probability of rigid triaxial shapes in nuclear ground states or at low angular momentum, for which there is somewhat scarce experimental evidence. The Tc isotopes, with the proton Fermi level just below the $Z = 50$ closed shell, belong to a region that can be considered as typical transitional nuclei which may exhibit γ softness or even well-developed triaxial shapes in the ground-state bands [1]. Evidence for a triaxial ground state in ^{98}Mo (the even-even “core” of ^{99}Tc) has previously been obtained from a study employing multiple Coulomb excitation [12]. In the odd- A Tc isotopic chain, the semi-magic ^{93}Tc nucleus with $N = 50$ is of spherical shape, while stable quadrupole deformation is expected to occur on the neutron-rich side because of the enhanced quadrupole correlation between valence nuclei occupying the proton $g_{9/2}$ and neutron $d_{5/2}$ orbitals. In earlier work, the level structures with positive and negative parity for several odd- A Tc nuclei in this region have been reported, including ^{95}Tc [13,14], ^{97}Tc [15,16], ^{101}Tc [17–19], ^{103}Tc [20], and $^{105-109}\text{Tc}$ [21]. Backbending caused by quasiparticle alignments was observed

in ^{97}Tc [16], ^{101}Tc [17,19], and $^{105,107,109}\text{Tc}$ [21]. The large signature splitting observed in the $g_{9/2}$ band in this region was associated with a large γ deformation [22].

The ^{99}Tc nucleus with $Z = 43$ and $N = 56$ is located at the middle of the transitional region and is expected to be another good candidate for triaxial deformation. The low-spin states in this nucleus have been investigated by β decay from ^{99}Mo [23–25]. States with higher spins have been populated via the $^{96}\text{Zr}(^6\text{Li}, 3n)^{99}\text{Tc}$ reaction [26,27] and the $^{98}\text{Mo}(^3\text{He}, pn)^{99}\text{Tc}$ reaction [28]. In those works, excited levels in ^{99}Tc were observed up to around 3 MeV and some collective levels were identified. However, high-spin data on ^{99}Tc were still lacking and no backbending in this nucleus was reported until now.

In this article, we present new experimental results on high-spin states in ^{99}Tc , enabling us to draw firm conclusions regarding also the low-spin character of the corresponding band structures. The collective bands are extended and expanded. Backbending and signature inversion are observed in the positive-parity band. Many new levels and transitions are identified and the electromagnetic properties of the structures are deduced. The results are compared with the total Routhian surface, the triaxial particle-rotor model, and semiclassical calculations of the electromagnetic properties.

II. EXPERIMENT AND RESULTS

The high-spin states of ^{99}Tc have been investigated through the fusion-evaporation reaction $^{96}\text{Zr}(^7\text{Li}, 4n)^{99}\text{Tc}$. The experiment was carried out at the China Institute of Atomic Energy (CIAE). The ^7Li beam was provided by the HI-13 tandem accelerator of CIAE, bombarding an enriched 86% ^{96}Zr target with 1.85 mg/cm^2 areal density. Excitation function measurements were performed in the energy range of 32–38 MeV and the beam energy of 35 MeV was found

* xiaozg@tsinghua.edu.cn

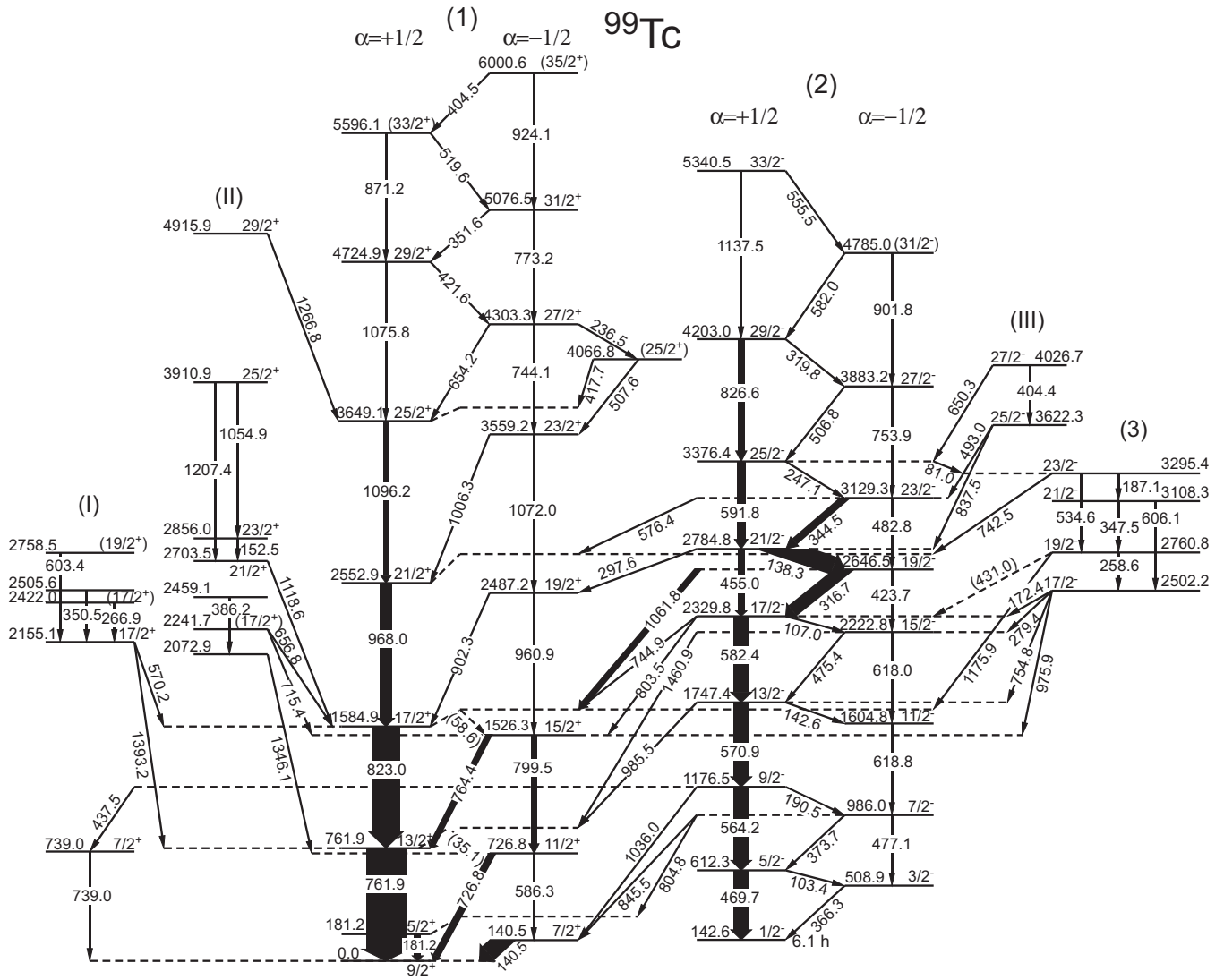


FIG. 1. The level scheme of ^{99}Tc deduced from the present work. The widths of the arrows are proportional to the relative intensities of the transitions. The energies are in keV.

to maximize the population of the $4n$ channel. The target was prepared by evaporating ZrO_2 powder onto a 10.3 mg/cm^2 lead backing. For the in-beam γ -ray measurement, a detector array was used with eight Compton-suppressed HPGe detectors, two planar HPGe detectors, and one clover detector. The detectors were placed at the angles of 40° , 90° , and 140° , respectively, with respect to the beam direction. Energy and efficiency calibrations of the detectors were done with ^{60}Co , ^{133}Ba , and ^{152}Eu standard sources before and after the irradiation. The total photopeak efficiency of the detector array at 1 MeV γ ray was about 0.3%. Coincidences were recorded event by event on hard drives with a time resolution of 15 ns. The offline data were sorted into $4\text{k} \times 4\text{k}$ channel matrices. A $E_\gamma - E_\gamma$ coincidence symmetric matrix was constructed to build the level scheme of ^{99}Tc . Two asymmetric matrices, with the 90° detectors sorted on one axis and the other Compton-suppressed HPGe detectors on the other axis, have been built to obtain the directional correlation of oriented state (DCO) ratios. A total of 3.7×10^7 coincident events were collected after subtraction

of background. The coincidence data were analyzed with the RADWARE software package [29].

The level scheme of ^{99}Tc obtained in the present work is shown in Fig. 1. It was deduced from the $\gamma - \gamma$ coincidences, the relative transition intensities, and a DCO-ratio analysis. Three collective band structures are labeled on the top of the bands with numbers (1)–(3), respectively. Three clusters of single-particle levels are also labeled with the numbers (I)–(III), respectively. For the bands (1) and (2), the signature components with $\alpha = +1/2$ and $\alpha = -1/2$ are also labeled at the top of each signature band. Compared with the previous results [23–28], the level scheme of ^{99}Tc was extended and expanded considerably in the present work. A total of 21 new levels and 60 new transitions are identified. The quality of the data is illustrated in Fig. 2, where the coincident γ -ray spectrum is obtained by gating on the 761.9-keV γ transition, from which all the corresponding γ transitions above the 761.9-keV energy level can be seen, except for some very weak transitions, such as the 58.6-, 81.0-, 431.0-, and 555.5-keV γ

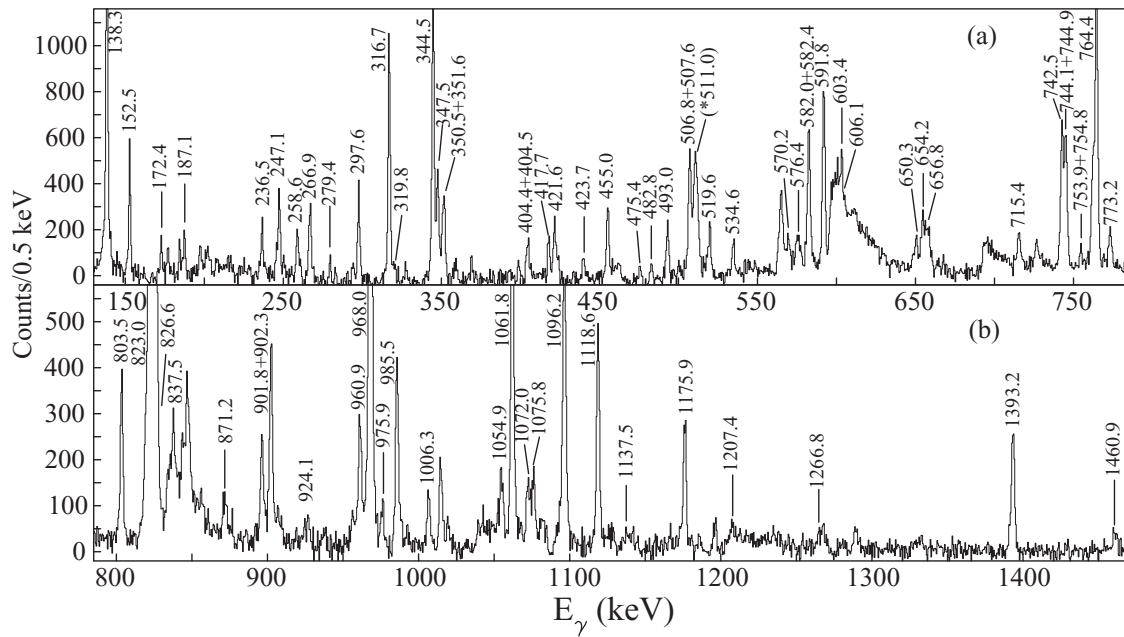


FIG. 2. The γ -ray spectrum obtained by a gate on the 761.9-keV γ transition in ^{99}Tc . The range of the energy is (a) from 130 to 785 keV, and (b) from 785 to 1470 keV.

rays. Figure 3 shows gates on γ -ray transitions in band (2). Figure 3(a) is gated on the 344.5-keV γ transition in band (2), from which one can see all the γ transitions in band (2) except

the parallel 591.8- and 482.8-keV transitions. Interestingly, the predominantly $M1$ transitions of 138.3, 316.7, and 344.5 keV are quite strong as compared with those above $I^\pi=23/2^-$

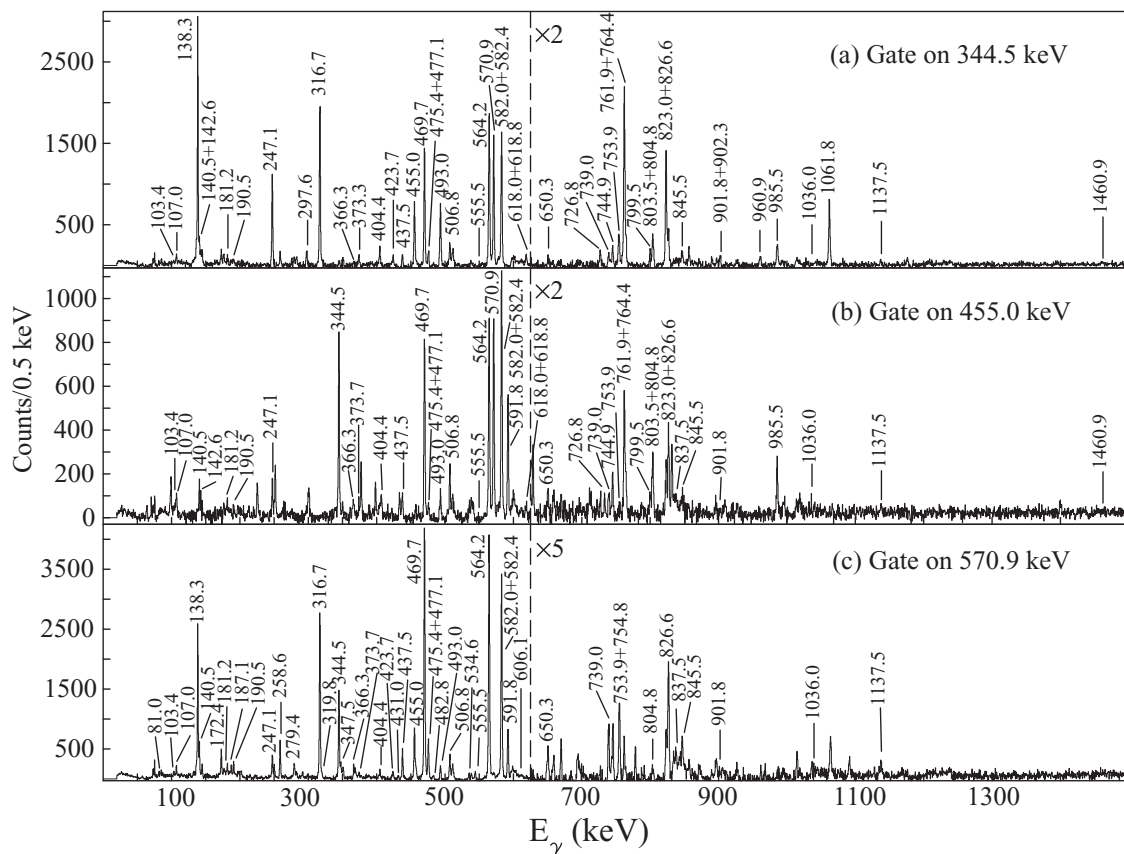


FIG. 3. The γ -ray spectra obtained by gating on the (a) 344.5-keV γ transition (b) 455.0-keV γ transition, and (c) 570.9-keV γ transition in ^{99}Tc .

and below $I^\pi=17/2^-$. The linking transitions below the 2784.8-keV level between bands (1) and (2), the 404.4-keV γ transition in cluster (III), as well as the linking transitions of 650.3- and 493.0-keV γ rays can also be seen in this figure. Figure 3(b) is obtained by gating on the 455.0-keV γ transition, from which, e.g., the strong $M1$ transitions of 138.3 and 316.7 keV are absent as expected. The linking transitions between band (2) and cluster (III) and those between bands (1) and (2) below the 2329.8-keV level are also marked in Fig. 3(b). Figure 3(c) shows a spectrum obtained by gating on the 570.9-keV γ transition, from which the transitions in band (3) as well as the linking transitions from band (3) to band (2) can be seen. However, the transitions in band (3) cannot be seen in the gated spectra of Figs. 3(a) and 3(b), confirming that band (3) feeds into band (2) below the $21/2^-$ level.

A summary of γ -ray energies, relative intensities, DCO ratios, multipolarities, the spin-parity assignments, as well as the corresponding level energies of ^{99}Tc are given in Table I. The DCO ratios were obtained by gating on stretched quadrupole γ -ray transitions. The DCO ratio for a pure stretched quadrupole transition is expected to be around 1.0, while the corresponding value for a pure stretched dipole transition is around 0.5 [30]. Some unobserved feeding transitions can be responsible for the intensity imbalance of the 140.5-keV level, similar to the observations in Refs. [26–28].

In Refs. [26–28], band (1) was assigned as a positive-parity band with spins up to $25/2^+$ at the 3649.1-keV level in the $\alpha = +1/2$ signature component and up to $15/2^+$ at 1526.3 keV in the $\alpha = -1/2$ signature component. We have extended this band up to the $33/2^+$ and $35/2^+$ states for the two signature components, respectively. Seven new levels with 4724.9 keV ($29/2^+$) and 5596.1 keV ($33/2^+$) in the $\alpha = +1/2$ signature component and 2487.2 keV ($19/2^+$), 3559.2 keV ($23/2^+$), 4303.3 keV ($27/2^+$), 5076.5 keV ($31/2^+$), and 6000.6 keV ($35/2^+$) in the $\alpha = -1/2$ signature component have been identified. Seven new $\Delta I = 2$ γ transitions, 1075.8 and 871.2 keV in the $\alpha = +1/2$ signature component, and 960.9, 1072.0, 744.1, 773.2, and 924.1 keV in the $\alpha = -1/2$ signature component, along with seven $\Delta I = 1$ γ transitions 35.1, 58.6, 654.2, 421.6, 351.6, 519.6, and 404.5 keV between the $\alpha = +1/2$ and the $\alpha = -1/2$ signature components have been newly identified. Band (2) was assigned as a negative-parity band with spins up to $25/2^-$ at the 3376.4-keV level in the $\alpha = +1/2$ signature component and $11/2^-$ at the 1604.8-keV level in the $\alpha = -1/2$ signature [26–28]. We have extended this band with spins up to $33/2^-$ at the 5340.5-keV level in the $\alpha = +1/2$ signature component and $31/2^-$ for the 4785.0-keV level in the $\alpha = -1/2$ signature component. Seven new levels with 4203.0 keV ($29/2^-$) and 5340.5 keV ($33/2^-$) in the $\alpha = +1/2$ signature and 2222.8 keV ($15/2^-$), 2646.5 ($19/2^-$) keV, 3129.3 keV ($23/2^-$), 3883.2 ($27/2^-$) keV, and 4785.0 keV ($31/2^-$) in the $\alpha = -1/2$ signature have been identified. Seven $\Delta I = 2$ transitions, 826.6 and 1137.5 keV in the $\alpha = +1/2$ signature, and 618.0, 423.7, 482.8, 753.9, and 901.8 keV in the $\alpha = -1/2$ signature, along with five $\Delta I = 1$ transitions 142.6, 107.0, 319.8, 582.0, and 555.5 keV between $\alpha = +1/2$ and $\alpha = -1/2$ signature have also been identified. The six $\Delta I = 1$ transitions 475.4, 316.7, 138.3, 344.5, 247.1, and 506.8 keV,

which have been previously observed in Refs. [26–28] are placed in band (2) as $M1/E2$ transitions according to the DCO ratios measured in this experiment. A side band (3) with weak population was identified. Based on the linking transitions of 172.4, 279.4, 754.8, and 975.9 keV between the 2502.2-keV level and bands (1) and (2), as well as the DCO ratios shown in Table I, the band head of band (3) is tentatively assigned as the 2502.2-keV level with spin and parity of $17/2^-$. In addition, several levels and transitions in clusters (I)–(III), and many new linking transitions between the bands and clusters have been identified.

III. DISCUSSION

In Ref. [28], states belonging to the positive-parity band (1) were assigned as the $\pi 5/2^+[422]$ configuration with the 181.2-keV ($5/2^+$) band head level, and the negative band (2) was assigned as built on the $\pi 1/2^-[301]$ configuration based on the 142.6-keV ($1/2^-$) level which is a 6.1-h isomer [25]. Examining the positive-parity band (1) in ^{99}Tc , at low-spin states, that is, the $5/2^+$, $7/2^+$ and $9/2^+$ states, a level order inversion happens compared with a regular rotational structure.

The ^{99}Tc nucleus is located in the $A \sim 100$ transitional region between spherical and well-deformed ground-state shapes. No collective band structures have been found in this region for the $N \leq 50$ odd- A ^{89}Tc [31], ^{91}Tc [32], and ^{93}Tc [33,34]. However, in the $N \geq 52$ odd- A $^{95-103}\text{Tc}$ isotopes, collective bands were observed. In the observed $\pi 5/2^+[422]$ and $\pi 1/2^-[301]$ bands, the transition intensities of the $\alpha = +1/2$ signature component are much stronger than those of the $\alpha = -1/2$ one. The systematic comparisons of the levels for the $\pi 5/2^+[422]$ bands in ^{99}Tc from the present work and in odd- A ^{95}Tc [13,14], ^{97}Tc [15,16], ^{101}Tc [17–19], and ^{103}Tc [20] are shown in Fig. 4. Figure 5 shows the level systematics for the $\pi 1/2^-[301]$ band in ^{99}Tc from the present work and in odd- A ^{95}Tc [13,14], ^{97}Tc [15,16], and ^{101}Tc [17,18,20]. For the ^{101}Tc nucleus, the levels of the $\pi 1/2^-[301]$ band reported in Ref. [18] have been reassigned in Ref. [20]. We agree with that reassignment as shown in Fig. 5. Comparing the level structures, one can see that the observed positive- and negative-parity bands in ^{99}Tc agree with the systematics, showing a similar structural character. From these two figures, a general observation can be used: The level energies with the same spin decrease systematically with increasing neutron number N . In the $\pi 5/2^+[422]$ bands, the level order inversion for the low-spin states is systematically reduced as the neutron number increases, disappearing for ^{103}Tc . These effects are probably caused by the deformation parameter (β_2) increasing and the Coriolis interaction decreasing with increasing neutron number in these Tc isotopes [28].

To understand the structural characteristics of band (1), total Routhian surface (TRS) calculations [35,36] have been performed. The TRS calculations are sensitive to a specific nucleonic configuration and will show, for each rotational frequency, the total energy in the rotating frame (Routhian) as a function of the deformation parameters β_2 , β_4 , and γ . A minimum in such a surface indicates the favored deformation for a specific configuration of the nucleus at a specific rotational frequency. The results for different frequencies are

TABLE I. The energies, relative intensities, DCO ratios, multiplicities, and spin-parity assignments of the γ -ray transitions and levels in ^{99}Tc . The * denotes the γ transitions newly identified in this work.

E_γ (keV)	Intensity(%)	E_i (keV)	E_f (keV)	Assignment	R_{DCO}	Multiplicity
(35.1)(2)*		761.9	726.8	$13/2^+ \rightarrow 11/2^+$		(M1/E2)
(58.6)(2)*		1584.9	1526.3	$17/2^+ \rightarrow 15/2^+$		(M1/E2)
81.0(2)*	8.1(17)	3376.4	3295.4	$25/2^- \rightarrow 23/2^-$		(M1/E2)
103.4(1)	2.8(10)	612.3	508.9	$5/2^- \rightarrow 3/2^-$		(M1/E2)
107.0(1)*	4.7(15)	2329.8	2222.8	$17/2^- \rightarrow 15/2^-$		(M1/E2)
138.3(2)	44.1(61)	2784.8	2646.5	$21/2^- \rightarrow 19/2^-$	1.32(10)	M1/E2
140.5(1)	43.2(6)	140.5	0.0	$7/2^+ \rightarrow 9/2^+$	1.40(20)	M1/E2
142.6(1)*	2.4(8)	1747.4	1604.8	$13/2^- \rightarrow 11/2^-$		(M1/E2)
152.5(1)	5.0(12)	2856.0	2703.5	$23/2^+ \rightarrow 21/2^+$	1.25(13)	M1/E2
172.4(1)*	8.1(5)	2502.2	2329.8	$17/2^- \rightarrow 17/2^-$	0.84(9)	(M1/E2)
181.2(1)	11.4(3)	181.2	0.0	$5/2^+ \rightarrow 9/2^+$	0.55(9)	M1/E2
187.1(1)*	2.8(9)	3295.4	3108.3	$23/2^- \rightarrow 21/2^-$		(M1/E2)
190.5(1)	2.2(6)	1176.5	986.0	$9/2^- \rightarrow 7/2^-$	0.77(11)	M1/E2
236.5(1)*	2.2(13)	4303.3	4066.8	$27/2^+ \rightarrow (25/2^+)$		(M1/E2)
247.1(1)	5.4(20)	3376.4	3129.3	$25/2^- \rightarrow 23/2^-$	0.51(6)	M1/E2
258.6(1)*	5.2(5)	2760.8	2502.2	$19/2^- \rightarrow 17/2^-$	0.46(4)	M1/E2
266.9(2)*	2.3(7)	2422.0	2155.1	$(17/2^+) \rightarrow 17/2^+$	0.72(12)	(M1/E2)
279.4(1)*	4.0(4)	2502.2	2222.8	$17/2^- \rightarrow 15/2^-$	0.65(7)	M1/E2
297.6(1)*	2.9(11)	2784.8	2487.2	$21/2^- \rightarrow 19/2^+$	0.61(9)	E1
316.7(1)	30.0(29)	2646.5	2329.8	$19/2^- \rightarrow 17/2^-$	0.51(2)	M1/E2
319.8(2)*	1.0(6)	4203.0	3883.2	$29/2^- \rightarrow 27/2^-$		(M1/E2)
344.5(1)	14.9(19)	3129.3	2784.8	$23/2^- \rightarrow 21/2^-$	0.65(5)	M1/E2
347.5(1)*	3.3(6)	3108.3	2760.8	$21/2^- \rightarrow 19/2^-$	0.66(9)	M1/E2
350.5(2)*	2.5(6)	2505.6	2155.1			
351.6(2)*	1.5(9)	5076.5	4724.9	$31/2^+ \rightarrow 29/2^+$	0.58(8)	M1/E2
366.3(1)	3.4(2)	508.9	142.6	$3/2^- \rightarrow 1/2^-$	0.64(10)	M1/E2
373.7(1)	2.5(1)	986.0	612.3	$7/2^- \rightarrow 5/2^-$	0.48(4)	M1/E2
386.2(2)*	1.2(6)	2459.1	2072.9			
404.4(2)*	1.3(4)	4026.7	3622.3	$27/2^- \rightarrow 15/2^-$		(M1/E2)
404.5(2)*	<1	6000.6	5596.1	$(35/2^+) \rightarrow (33/2^+)$		(M1/E2)
417.7(1)*	1.2(5)	4066.8	3649.1	$25/2^+ \rightarrow (25/2^+)$		(M1/E2)
421.6(2)*	1.6(6)	4724.9	4303.3	$29/2^+ \rightarrow 27/2^+$	0.72(11)	M1/E2
423.7(2)*	2.1(9)	2646.5	2222.8	$19/2^- \rightarrow 15/2^-$	0.91(11)	E2
(431.0)(3)*	<1	2760.8	2329.8	$19/2^- \rightarrow 17/2^-$		(M1/E2)
437.5(2)	3.5(1)	1176.5	739.0	$9/2^- \rightarrow 7/2^+$	0.56(5)	E1
455.0(1)	12.4(21)	2784.8	2329.8	$21/2^- \rightarrow 17/2^-$	0.99(6)	E2
469.7(1)	35.6(4)	612.3	142.6	$5/2^- \rightarrow 1/2^-$	0.95(3)	E2
475.4(1)	5.2(11)	2222.8	1747.4	$15/2^- \rightarrow 13/2^-$	0.72(5)	M1/E2
477.1(1)	1.7(1)	986.0	508.9	$7/2^- \rightarrow 3/2^-$		(E2)
482.8(2)*	1.7(9)	3129.3	2646.5	$23/2^- \rightarrow 19/2^-$		(E2)
493.0(1)	3.9(16)	3622.3	3129.3	$25/2^- \rightarrow 23/2^-$	1.23(17)	M1/E2
506.8(1)	8.8(29)	3883.2	3376.4	$27/2^- \rightarrow 25/2^-$	0.65(5)	M1/E2
507.6(2)*	1.1(4)	4066.8	3559.2	$(25/2^+) \rightarrow 23/2^+$		(M1/E2)
519.6(2)*	1.2(9)	5596.1	5076.5	$(33/2^+) \rightarrow 31/2^+$		(M1/E2)
534.6(1)*	2.8(7)	3295.4	2760.8	$23/2^- \rightarrow 19/2^-$	0.91(13)	E2
555.5(2)*	<1	5340.5	4785.0	$33/2^- \rightarrow 31/2^-$		(M1/E2)
564.2(1)	35.1(4)	1176.5	612.3	$9/2^- \rightarrow 5/2^-$	1.05(3)	E2
570.2(4)*	1.1(4)	2155.1	1584.9	$17/2^+ \rightarrow 17/2^+$	0.86(13)	M1/E2
570.9(1)	36.0(27)	1747.4	1176.5	$13/2^- \rightarrow 9/2^-$	0.95(3)	E2
576.4(3)*	<1	3129.3	2552.9	$23/2^- \rightarrow 21/2^+$		(E1)
582.0(2)*	<1	4785.0	4203.0	$(31/2^-) \rightarrow 29/2^-$		(M1/E2)
582.4(2)	36.7(32)	2329.8	1747.4	$17/2^- \rightarrow 13/2^-$	1.00(3)	E2
586.3(1)	2.3(9)	726.8	140.5	$11/2^+ \rightarrow 7/2^+$	0.97(11)	E2
591.8(1)	17.8(27)	3376.4	2784.8	$25/2^- \rightarrow 21/2^-$	0.96(8)	E2
603.4(2)*	2.2(4)	2758.5	2155.1	$(19/2^+) \rightarrow 17/2^+$	0.80(14)	(M1/E2)
606.1(2)*	1.7(8)	3108.3	2502.2	$21/2^- \rightarrow 17/2^-$		(E2)

TABLE I. (*Continued.*)

E_γ (keV)	Intensity(%)	E_i (keV)	E_f (keV)	Assignment	R_{DCO}	Multipolarity
618.0(2)*	1.6(10)	2222.8	1604.8	$15/2^- \rightarrow 11/2^-$		(E2)
618.8(2)	4.2(16)	1604.8	986.0	$11/2^- \rightarrow 7/2^-$		(E2)
650.3(2)*	1.9(14)	4026.7	3376.4	$27/2^- \rightarrow 25/2^-$	0.56(8)	M1/E2
654.2(2)*	1.8(6)	4303.3	3649.1	$27/2^+ \rightarrow 25/2^+$	0.70(9)	M1/E2
656.8(5)*	1.0(3)	2241.7	1584.9	$(17/2^+) \rightarrow 17/2^+$	0.59(5)	M1/E2
715.4(3)*	1.9(6)	2241.7	1526.3	$(17/2^+) \rightarrow 15/2^+$	0.86(13)	(M1/E2)
726.8(1)	14.0(3)	726.8	0.0	$11/2^+ \rightarrow 9/2^+$	1.21(8)	M1/E2
739.0(1)	4.6(2)	739.0	0.0	$7/2^+ \rightarrow 9/2^+$	0.76(8)	M1/E2
742.5(1)	6.1(11)	3295.4	2552.9	$23/2^- \rightarrow 21/2^+$	0.61(5)	E1
744.1(3)*	<1	4303.3	3559.2	$27/2^+ \rightarrow 23/2^+$		(E2)
744.9(2)*	5.9(10)	2329.8	1584.9	$17/2^- \rightarrow 17/2^+$	0.61(5)	E1
753.9(2)*	1.9(13)	3883.2	3129.3	$27/2^- \rightarrow 23/2^-$		(E2)
754.8(1)*	4.8(5)	2502.2	1747.4	$17/2^- \rightarrow 13/2^-$	1.10(11)	E2
761.9(1)	100	761.9	0.0	$13/2^+ \rightarrow 9/2^+$	1.06(2)	E2
764.4(1)	12.0(15)	1526.3	761.9	$15/2^+ \rightarrow 13/2^+$	1.04(5)	M1/E2
773.2(2)*	1.9(15)	5076.5	4303.3	$31/2^+ \rightarrow 27/2^+$		(E2)
799.5(1)	10.0(3)	1526.3	726.8	$15/2^+ \rightarrow 11/2^+$	1.07(13)	E2
803.5(1)	7.7(21)	2329.8	1526.3	$17/2^- \rightarrow 15/2^+$	0.69(8)	E1
804.8(2)	1.0(5)	986.0	181.2	$7/2^- \rightarrow 5/2^+$		(E1)
823.0(1)	67.6(7)	1584.9	761.9	$17/2^+ \rightarrow 13/2^+$	0.98(2)	E2
826.6(3)*	12.2(14)	4203.0	3376.4	$29/2^- \rightarrow 25/2^-$	0.96(7)	E2
837.5(2)*	1.8(9)	3622.3	2784.8	$15/2^- \rightarrow 21/2^-$		(E2)
845.5(2)	1.3(6)	986.0	140.5	$7/2^- \rightarrow 7/2^+$		(E1)
871.2(2)*	2.1(19)	5596.1	4724.9	$33/2^+ \rightarrow 29/2^+$		(E2)
901.8(3)*	<1	4785.0	3883.2	$31/2^- \rightarrow 27/2^-$		(E2)
902.3(1)	5.0(10)	2487.2	1584.9	$19/2^+ \rightarrow 17/2^+$	0.86(8)	M1/E2
924.1(3)	<1	6000.6	5076.5	$(35/2^+) \rightarrow 31/2^+$		(M1/E2)
960.9(1)*	5.4(14)	2487.2	1526.3	$19/2^+ \rightarrow 15/2^+$	1.09(13)	E2
968.0(1)	26.0(25)	2552.9	1584.9	$21/2^+ \rightarrow 17/2^+$	1.04(4)	E2
975.9(2)*	2.6(11)	2502.2	1526.3	$17/2^- \rightarrow 15/2^+$		(E1)
985.5(1)	8.7(3)	1747.4	761.9	$13/2^- \rightarrow 13/2^+$	1.05(10)	E1
1006.3(3)*	1.7(7)	3559.2	2552.9	$23/2^+ \rightarrow 21/2^+$	0.80(11)	M1/E2
1036.0(3)*	1.3(8)	1176.5	140.5	$9/2^- \rightarrow 7/2^+$		(E1)
1054.9(2)*	1.4(8)	3910.9	2856.0	$25/2^+ \rightarrow 23/2^+$	1.14(20)	M1/E2
1061.8(1)	11.7(18)	2646.5	1584.9	$19/2^- \rightarrow 17/2^+$	0.56(4)	E1
1072.0(2)*	2.6(12)	3559.2	2487.2	$23/2^+ \rightarrow 19/2^+$	0.96(16)	E2
1075.8(2)*	1.9(8)	4724.9	3649.1	$29/2^+ \rightarrow 25/2^+$	0.92(15)	E2
1096.2(1)	10.2(17)	3649.1	2552.9	$25/2^+ \rightarrow 21/2^+$	0.95(6)	E2
1118.6(1)	6.5(13)	2703.5	1584.9	$21/2^+ \rightarrow 17/2^+$	1.04(8)	E2
1137.5(2)*	2.1(13)	5340.5	4203.0	$33/2^- \rightarrow 29/2^-$	1.10(17)	E2
1175.9(2)	4.2(11)	2760.8	1584.9	$19/2^- \rightarrow 17/2^+$	0.64(6)	E1
1207.4(3)*	1.1(7)	3910.9	2703.5	$25/2^+ \rightarrow 21/2^+$	1.09(31)	E2
1266.8(3)*	1.2(8)	4915.9	3649.1	$29/2^+ \rightarrow 25/2^+$	1.06(22)	E2
1346.1(2)*	2.5(2)	2072.9	726.8			
1393.2(2)	6.1(2)	2155.1	761.9	$17/2^+ \rightarrow 13/2^+$	0.96(9)	E2
1460.9(2)*	4.0(2)	2222.8	761.9	$15/2^- \rightarrow 13/2^+$		(E1)

shown in Fig. 6. As indicated in Fig. 6, the TRS calculations predict a well-developed triaxial minimum with deformation parameters ($\beta_2 = 0.19$, $\gamma = -30^\circ$) for the yrast positive-parity configuration. When the rotational frequency changes from 0.2 to 0.5 MeV, the deformation parameter β_2 stays approximately constant and the change in γ is also quite small, from -30° to -35° . The predicted triaxiality of the $A \sim 100$ Tc isotopes is illustrated by the systematical comparison of calculations performed at $\hbar\omega = 0.2$ MeV shown in Fig. 7. The results of

the TRS calculations indicate a transition from a near-spherical to a triaxial-deformed shape when the neutron number varies from $N = 50$ to $N = 60$. The quadrupole deformation also becomes larger when more neutrons are added to the $N = 50$ closed shell. Triaxiality is predicted to appear in ^{97}Tc and to be more developed in $^{99,101,103}\text{Tc}$.

The staggering parameter $S(I)$ with the form of $S(I) = [E(I) - E(I-1)]/I$ is derived experimentally for band (1) and plotted as a function of the spin I in Fig. 8. It is

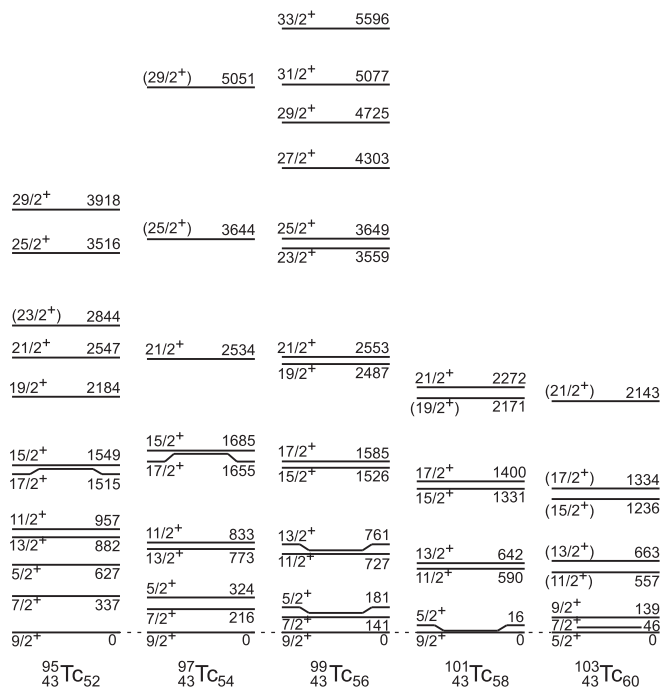


FIG. 4. The energy level systematics for the $5/2^+$ [422] bands in odd- A $^{95-103}\text{Tc}$.

evident that large signature splitting occurs, particularly before the backbending at approximately $I = 27/2\hbar$. After the backbending, signature inversion appears around $I = 29/2\hbar$.

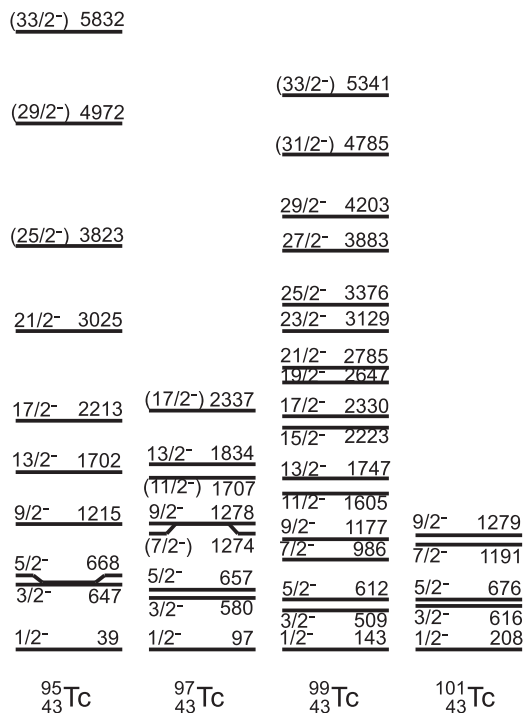


FIG. 5. The energy level systematics for the $1/2^-$ [301] bands in odd- A $^{95-101}\text{Tc}$. The energies of the $1/2^-$ states have been taken as a reference.

Around this spin value, the large signature splitting disappears. It could be caused by the alignment of a pair of $h_{11/2}$ neutrons (as will be discussed below), which forces an initially large γ value towards axial symmetry [37].

To further investigate the effects of a triaxial shape on the ground-state rotational structure built on the $\pi g_{9/2}[422]5/2^+$ configuration, quasi-particle-rotor model (PRM) calculations for the axial as well as triaxial deformation are presented (see Fig. 8). PRM calculations [38] have been performed with the predicted deformation parameters β_2 and β_4 taken from the TRS predictions. The standard parameter set [39] of the Nilsson model is used and the moment of inertia from the neighboring ^{98}Mo “core” is considered to account for the bulk properties of the band. It should be noted that the ^{98}Mo “core” used in the calculation is reported to be triaxial in the ground state [12]. The obtained staggering at different attenuation of the Coriolis interactions ρ and triaxial deformation γ are presented in Fig. 8. The energy staggering is reproduced reasonably well by both the axial symmetry and triaxiality. However, for the $I = 7/2\hbar$ state, only $\gamma = 0^\circ$ is able to reproduce the trend.

Although the overall staggering pattern is reproduced, it is interesting to consider in more detail the energy level sequence to draw a conclusion. Figure 9 shows the influence of the Coriolis interaction ρ and triaxial deformation parameter γ on the calculated energy spectra. Good agreement with the measured values can be seen at low spins for an axial symmetric shape with the Coriolis attenuation parameter $\rho = 0.6$; however, discrepancy at higher spins is visible. Introducing the triaxiality in the deformed basis (see the right part of Fig. 9), the calculated levels agree better with the experimental ones at higher spins. Hence, the PRM analysis suggests a transition from an axial symmetric shape at low angular momentum to a triaxial shape in the high spin part of the ground-state band structure.

Figure 10 shows the total rotation-aligned angular momentum I_x as a function of the rotational frequency $\hbar\omega$ in bands (1) and (2) in ^{99}Tc , where we use the standard definitions $I_x = \sqrt{(I_a + 1/2)^2 - K^2}$, $I_a = (I_i + I_f)/2$, $\hbar\omega = (E_i - E_f)/[I_x(I_i) - I_x(I_f)]$. According to the configurations given above, we propose $K = 5/2$ and $K = 1/2$ for bands (1) and (2), respectively. One can see that backbending occurs at $\hbar\omega \sim 0.44$ MeV for band (1), which can be caused by the alignment of a pair of $h_{11/2}$ neutrons. Such neutron alignments have also been reported in odd- A technetium isotopes ^{101}Tc [17, 19], and $^{105,107,109}\text{Tc}$ [21]. For band (2), there is an increase of aligned angular momentum at $\hbar\omega \sim 0.26$ MeV. Around this rotational frequency, the intraband $M1$ transitions also become unusually strong. Different explanations may be proposed to explain this interesting observation. One possibility is that the structure above the 2646.5-keV ($19/2^-$) level is based on a different three-quasiparticle configuration, similar to band (4) in the isotone ^{101}Rh , which was assigned to be based on the $\pi g_{9/2} \otimes (d_{5/2}h_{11/2})$ configuration [40]. The total angular momentum alignment for band (4) in ^{101}Rh is also shown in Fig. 10, exhibiting a similar pattern to that of the higher spin states in band (2). Another scenario involves the mixing of the $p_{1/2}[301]1/2^-$ Nilsson orbital with the $f_{5/2}[301]3/2^-$ orbital at medium spins. The transition probabilities for interband $M1$

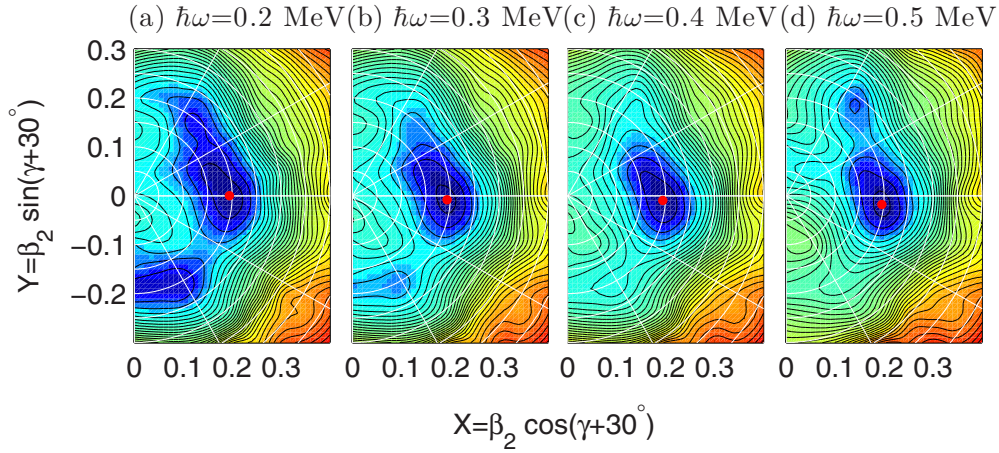


FIG. 6. (Color online) The TRS calculations for ^{99}Tc at $\hbar\omega = 0.2\text{--}0.5$ MeV with the proton orbital of positive parity and positive signature closest to the Fermi surface blocked. The successive contour curves denote a difference of 200 keV in energy.

transitions between the $3/2^- [301]$ and $1/2^- [301]$ bands would then be much larger than the pure intraband $M1$ transitions because they are spin-flip transitions [28]. The $[301]3/2^-$ band at low spins was reported in Ref. [28], however, it was not identified in the present work. A third possibility could be a shape change as discussed for ^{101}Tc in Ref. [17], suggesting that strong $M1$ transitions turning to strong $E2$ transitions at low spins is characteristic of a shape change. Clearly a deeper understanding of band (2) requires more theoretical work.

$B(M1)/B(E2)$ ratios can be analyzed to gain further insight into the proposed configurations for bands (1) and (2). The experimental ratios can be extracted using the following formula [41]:

$$\frac{B(M1; I \rightarrow I - 1)}{B(E2; I \rightarrow I - 2)} = 0.697 \frac{1}{\lambda} \frac{E_\gamma^5(E2)}{E_\gamma^3(M1)} \frac{1}{1 + \delta^2} \left[\frac{\mu_N^2}{e^2 b^2} \right], \quad (1)$$

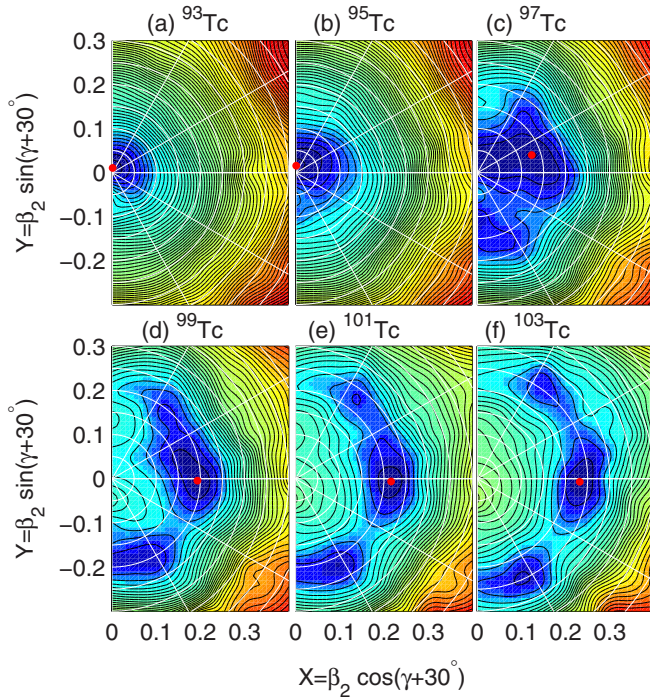


FIG. 7. (Color online) The systematical comparisons for TRS calculations in odd- A $^{93\text{--}103}\text{Tc}$ at $\hbar\omega = 0.2$ MeV with the proton orbital of positive parity and positive signature closest to the Fermi surface blocked. The successive contour curves denote a difference of 200 keV in energy.

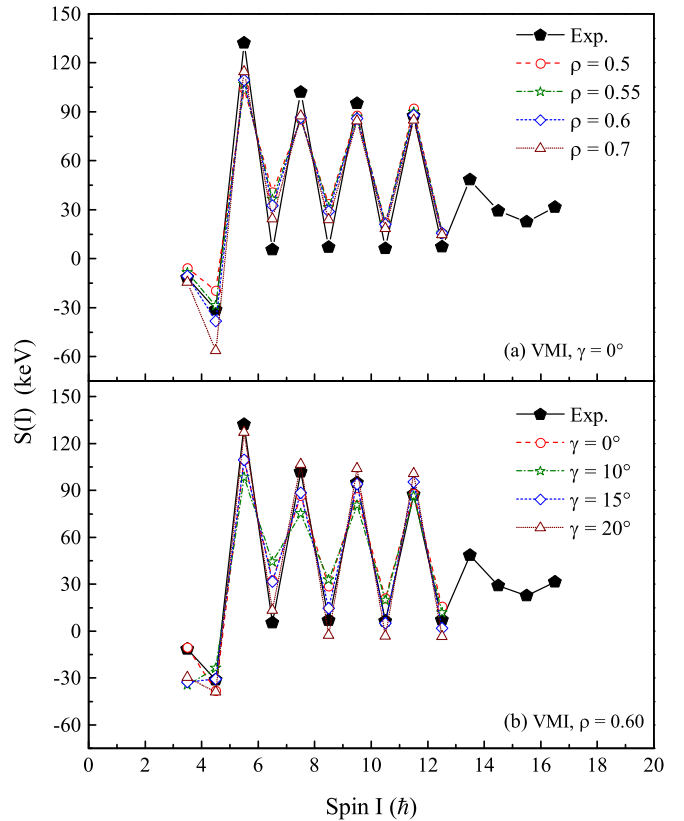


FIG. 8. (Color online) The energy staggering parameter $S(I)$ for the $5/2^+ [422]$ band in comparison with the particle-rotor model calculations in ^{99}Tc .

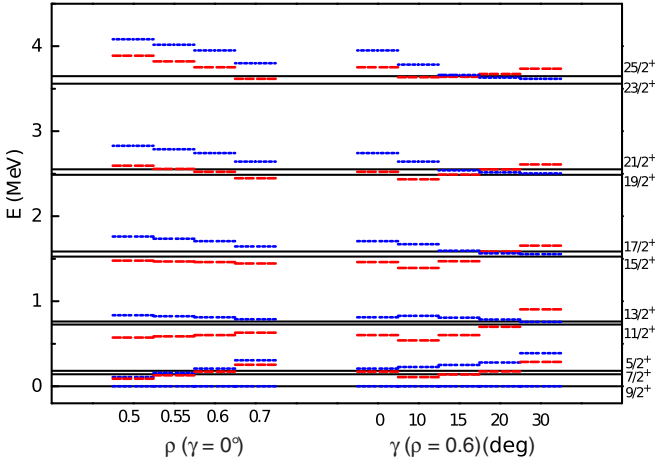


FIG. 9. (Color online) The comparison between experimental and calculated levels for the ground-state band in ^{99}Tc . Black (solid) lines across the plot are the experimental energies. Red (dashed) and blue (dotted) lines are calculated energies for the $\alpha = -1/2$ and $\alpha = +1/2$ signature, respectively.

where δ is the $E2$ admixture in the $M1$ transition and is set to zero in the calculation except for the 726.8- and 764.4-keV γ transitions. The δ values for the 726.8- and 764.4-keV γ transitions are taken from Ref. [27]. The energy is given in MeV. The experimental branching ratio λ is defined as $I(\Delta I = 2)/I(\Delta I = 1)$ with gates set on the transitions above the states of interest. The theoretical expression for the $B(M1)/B(E2)$ values within the semiclassical Dönau-Frauendorf model was applied using the formula [42,43],

$$\frac{B(M1; I \rightarrow I-1)}{B(E2; I \rightarrow I-2)} = \frac{12}{5Q_0^2 \cos^2(\gamma + 30^\circ)} \left[1 - \frac{K^2}{(I-1/2)^2} \right]^{-2} \left\{ \left(1 - \frac{K^2}{I^2} \right) \right. \\ \times \left[\Omega_1 (g_1 - g_R) \left(1 \pm \frac{\Delta e'}{\hbar\omega} \right) + \sum_n \Omega_n (g_n - g_R) \right] \\ \left. - \frac{K}{I} \left[(g_1 - g_R) i_p + \sum_n (g_n - g_R) i_n \right] \right\}^2 \left[\frac{\mu_N^2}{e^2 b^2} \right],$$

here Ω_1 , i_1 , and g_1 are the Ω value, alignment, and g factor for the particle causing the signature splitting, respectively, while Ω_n , i_n , and g_n refer to the Ω value, alignment, and g factor of the other quasiparticles involved in the configuration, respectively. The parameters $g_R = Z/A$ and $K = \sum_n \Omega_n$ denote the rotational g factor and total K value, respectively. A signature-dependent term is present for the particle that causes the splitting, where $\Delta e'$ is the experimental energy splitting between the routhians of the two signature partners. The $+$ ($-$) sign in the signature splitting term is for transitions from unfavored (favored) to favored (unfavored) signature. The quadrupole moment is given by the expression $Q_0 = \frac{3}{\sqrt{5\pi}} R^2 Z \beta_2 (1 + 0.16\beta_2)$. Here K , γ , and β_2 are set as 2.5, -30° , and 0.19 for band (1), and 0.5, -10° , and 0.16 for band (2), respectively, with the deformation parameters β_2

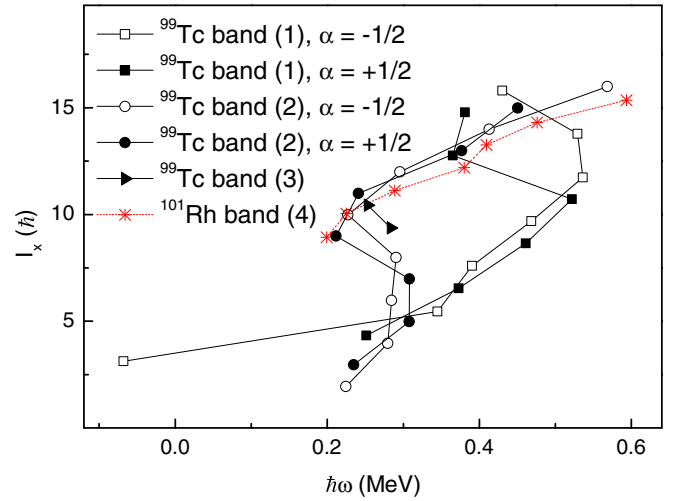


FIG. 10. (Color online) Experimental total angular momentum alignment I_x as a function of the rotational frequency for the positive- and the negative-parity bands in ^{99}Tc as well as band (4) in ^{101}Rh [40]. The open and solid symbols correspond to the $\alpha = +1/2$ and $\alpha = -1/2$ signatures, respectively.

and γ taken from the TRS calculations. The experimental $B(M1)/B(E2)$ ratios and the calculated results for bands (1) and (2) are shown in Figs. 11(a) and 11(b), respectively. For band (1), because of the large signature splitting, the semiclassical calculations both with and without considering the signature splitting factor are conducted, as shown by the

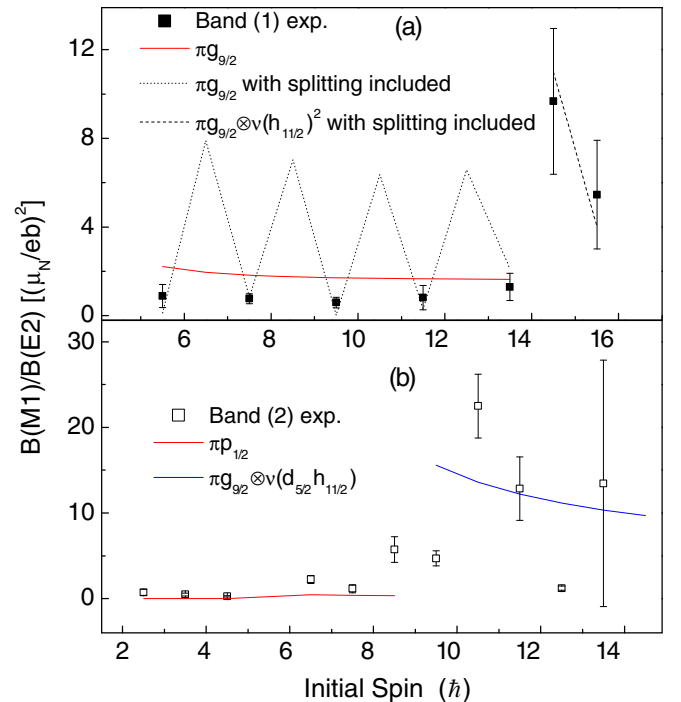


FIG. 11. (Color online) The experimental $B(M1)/B(E2)$ ratios as a function of spin in comparison with the calculations using the semiclassical Dönau-Frauendorf model for (a) band (1), and (b) band (2).

dashed and solid curves, respectively. However, the experimental results for the $\alpha = +1/2$ signature before backbending is missing because of the disappearance of connecting $M1$ transitions, while the alignment from a pair of $h_{11/2}$ neutrons is added for the configuration after the backbending, which fits the experimental data quite well. For band (2), the $\pi p_{1/2}$ orbital was used for the low spins, while the theoretical predictions for the $\pi g_{9/2} \otimes \nu(d_{5/2}h_{11/2})$ configuration is also plotted in the figure. However, because of the erratic experimental $B(M1)/B(E2)$ values at higher spins, the character of band (2) remains an open question for $I > 17/2 \hbar$.

Band (3) is identified for the first time in the present work and assigned as a negative-parity band according to the DCO measurements of the transitions. It may belong to a three-quasiparticle band. We note here that more work is needed to understand both band (3) and the clusters (I)–(III).

IV. SUMMARY

In summary, the structure of the ^{99}Tc nucleus was studied via the fusion-evaporation reaction $^{96}\text{Zr}(^7\text{Li}, 4n)^{99}\text{Tc}$ at 35 MeV. Sixty new γ transitions and 21 new energy levels were identified. Two collective bands built on the $\pi g_{9/2}[422]5/2^+$

and $\pi p_{1/2}[301]1/2^-$ configurations, respectively, have been expanded. One new weak band and some single-particle states were identified. The large signature splitting in the positive-parity band of ^{99}Tc is associated with large triaxiality at medium to high spins, which is supported by the TRS predictions, the electromagnetic properties [i.e., $B(M1)/B(E2)$ ratios], and the triaxial particle-rotor model calculations. The structural character of band (2) was discussed and more theoretical work is still needed to understand its high-spin structure.

ACKNOWLEDGMENTS

The work at Tsinghua University was supported by the National Natural Science Foundation of China under Grants No. 11175095 and No. 11375094, by Tsinghua University Initiative Scientific Research Program, and by the Special Program of Higher Education Science Foundation under Grant No. 2010000211007. B.C. and C.Q. are supported by the Swedish Research Council (VR) under Grants No. 621-2010-3694, No. 621-2012-3805, and No. 621-2013-4323. H.J.L. is supported in part by the China Scholarship Council under Grant No. 201306210205.

-
- [1] P. Möller, R. Bengtsson, B. G. Carlsson, P. Olivius, and T. Ichikawa, *Phys. Rev. Lett.* **97**, 162502 (2006).
- [2] J. A. Pinston, W. Urban, Ch. Droste, T. Rząca-Urban, J. Genevey, G. Simpson, J. L. Durell, A. G. Smith, B. J. Varley, and I. Ahmad, *Phys. Rev. C* **74**, 064304 (2006).
- [3] L. Gu *et al.*, *Chin. Phys. Lett.* **26**, 092502 (2009).
- [4] L. Gu *et al.*, *Phys. Rev. C* **79**, 054317 (2009).
- [5] J. J. Sun *et al.*, *Phys. Lett. B* **734**, 308 (2014).
- [6] S. P. Hu *et al.*, *Phys. Lett. B* **732**, 59 (2014).
- [7] Y. Toh *et al.*, *Phys. Rev. C* **87**, 041304(R) (2013).
- [8] S. W. Ødegård *et al.*, *Phys. Rev. Lett.* **86**, 5866 (2001).
- [9] R. F. Casten, E. A. McCutchan, N. V. Zamfir, C. W. Beausang, and J. Zhang, *Phys. Rev. C* **67**, 064306 (2003).
- [10] A. Bohr and B. R. Mottelson, *Nuclear Structure*, Vol. 2 (Benjamin, Reading, 1975).
- [11] N. V. Zamfir and R. F. Casten, *Phys. Lett. B* **260**, 265 (1991).
- [12] M. Zielińska *et al.*, *Nucl. Phys. A* **712**, 3 (2002).
- [13] G. Winter, F. Dönau, L. Funke, P. Kemnitz, and E. Will, *Nucl. Phys. A* **291**, 401 (1977).
- [14] S. S. Ghugre *et al.*, *Phys. Rev. C* **61**, 024302 (1999).
- [15] H. Aslan, B. Crowe, T. Dague, D. G. Savage, S. Zeghib, F. A. Rickey, and P. C. Simms, *Phys. Rev. C* **54**, 576 (1996).
- [16] D. Bucurescu, A. Gadea, Ghe. Căta-Danil, I. Căta-Danil, M. Ivaşcu, N. Mărginean, C. Rusu, L. Stroe, and C. A. Ur, *Eur. Phys. J. A* **16**, 469 (2003).
- [17] H. Dejbakhsh, G. Mouchaty, and R. P. Schmitt, *Phys. Rev. C* **44**, 119 (1991).
- [18] D. G. Savage, H. Aslan, B. Crowe, T. Dague, S. Zeghib, F. A. Rickey, and P. C. Simms, *Phys. Rev. C* **55**, 120 (1997).
- [19] F. Hoellinger *et al.*, *Eur. Phys. J. A* **4**, 319 (1999).
- [20] A. Bauchet *et al.*, *Eur. Phys. J. A* **10**, 145 (2001).
- [21] Y. X. Luo *et al.*, *Phys. Rev. C* **70**, 044310 (2004).
- [22] H.-J. Keller, S. Frauendorf, U. Hagemann, L. Käubler, H. Prade, and F. Stary, *Nucl. Phys. A* **444**, 261 (1985).
- [23] E. Bashandy and N. Ibrahiem, *Z. Phys.* **219**, 337 (1969).
- [24] W. B. Cook, L. Schellenberg, and M. W. Johns, *Nucl. Phys. A* **139**, 277 (1969).
- [25] P. L. Gardulski and M. L. Wiedenbeck, *Phys. Rev. C* **9**, 262 (1974).
- [26] K. O. Zell, H. Harter, D. Hippe, H. W. Schuh, and P. von Brentano, *Z. Phys. A* **316**, 351 (1984).
- [27] G. Kajrys, W. Del Bianco, S. Pilotte, S. Landsberger, and S. Monaro, *Phys. Rev. C* **31**, 409 (1985).
- [28] B. Crowe, H. Aslan, T. Dague, D. G. Savage, S. Zeghib, F. A. Rickey, and P. C. Simms, *Phys. Rev. C* **57**, 590 (1998).
- [29] D. C. Radford, *Nucl. Instrum. Methods Phys. Res., Sect. A* **361**, 297 (1995).
- [30] B. Singh and J. C. Waddington, [<http://www.nndc.bnl.gov/nndc/evalcorner/hijpi.pdf>].
- [31] D. Rudolph *et al.*, *Nucl. Phys. A* **587**, 181 (1995).
- [32] D. Rudolph *et al.*, *Phys. Rev. C* **49**, 66 (1994).
- [33] H. A. Roth, S. E. Arnell, D. Foltescu, Ö. Skeppstedt, J. Blomqvist, A. Nilsson, T. Kuroyanagi, S. Mitarai, and J. Nyberg, *Phys. Rev. C* **50**, 1330 (1994).
- [34] M. Hausmann *et al.*, *Phys. Rev. C* **68**, 024309 (2003).
- [35] W. Nazarewicz *et al.*, *Nucl. Phys. A* **503**, 285 (1989).
- [36] W. Satula and R. Wyss, *Phys. Scr.*, **T56**, 159 (1995).
- [37] D. R. Haenni, H. Dejbakhsh, R. P. Schmitt, and G. Mouchaty, *Phys. Rev. C* **33**, 1543 (1986).
- [38] S. E. Larsson, G. Leander, and I. Ragnarsson, *Nucl. Phys. A* **307**, 189 (1978).
- [39] T. Bengtsson and I. Ragnarsson, *Nucl. Phys. A* **436**, 14 (1985).
- [40] J. Timár *et al.*, *Nucl. Phys. A* **696**, 241 (2001).
- [41] C. W. Beausang, L. Hildingsson, E. S. Paul, W. F. Piel Jr., N. Xu, and D. B. Fossan, *Phys. Rev. C* **36**, 1810 (1987).
- [42] F. Dönau and S. Frauendorf, in *Proceedings of the Conference on High Angular Momentum Properties of Nuclei*, OakRidge, edited by N. R. Johnson (Harwood, New York, 1983), p. 143.
- [43] F. Dönau, *Nucl. Phys. A* **471**, 469 (1987).